J. Fluid Mech. (2014), *vol.* 760, *pp.* 278–303. © Cambridge University Press 2014
doi:10.1017/jfm.2014.586

Linear and nonlinear evolution of a localized disturbance in polymeric channel flow

Akshat Agarwal[1], Luca Brandt[2] and Tamer A. Zaki[1,†]

[1]Department of Mechanical Engineering, Imperial College London, London SW7 2AZ, UK

[2]Linné Flow Centre, SeRC, KTH Mechanics, Stockholm, SE-100 44, Sweden

(Received 13 April 2014; revised 13 August 2014; accepted 30 September 2014;
first published online 5 November 2014)

The evolution of an initially localized disturbance in polymeric channel flow is investigated, with the FENE-P model used to characterize the viscoelastic behaviour of the flow. In the linear growth regime, the flow response is stabilized by viscoelasticity, and the maximum attainable disturbance-energy amplification is reduced with increasing polymer concentration. The reduction in the energy growth rate is attributed to the polymer work, which plays a dual role. First, a spanwise polymer-work term develops, and is explained by the tilting action of the wall-normal vorticity on the mean streamwise conformation tensor. This resistive term weakens the spanwise velocity perturbation thus reducing the energy of the localized disturbance. The second action of the polymer is analogous, with a wall-normal polymer work term that weakens the vertical velocity perturbation. Its indirect effect on energy growth is substantial since it reduces the production of Reynolds shear stress and in turn of the streamwise velocity perturbation, or streaks. During the early stages of nonlinear growth, the dominant effect of the polymer is to suppress the large-scale streaky structures which are strongly amplified in Newtonian flows. As a result, the process of transition to turbulence is prolonged and, after transition, a drag-reduced turbulent state is attained.

Key words: non-Newtonian flows, transition to turbulence, viscoelasticity

1. Introduction

Transition to turbulence has been studied extensively in Newtonian channel flows due to its theoretical and practical importance. Previous numerical (Henningson, Lundbladh & Johansson 1993) and experimental (Breuer & Landahl 1990) studies have examined the transition process starting from three-dimensional, initially localized disturbances to model generic perturbations in the flow. The early stages of transition can be explained by appealing to linear theory, but nonlinear effects ultimately become important and give way to the onset of turbulence. Both the linear and nonlinear stages can, however, deviate from the Newtonian behaviour when small quantities of polymers are introduced in the flow. Previous linear theory has focused on the stability of a laminar base state, while the nonlinear efforts have focused on

† Present address: Department of Mechanical Engineering, Johns Hopkins University, Baltimore, MD 21218, USA. Email address for correspondence: t.zaki@jhu.edu

https://doi.org/10.1017/jfm.2014.586 Published online by Cambridge University Press

fully turbulent flows due to the propensity of the polymer to reduce drag (Toms 1948). The transition process, which includes the early linear dynamics and the subsequent nonlinear stages leading to turbulence, is examined herein using direct numerical simulations (DNS) of initially localized disturbances in polymeric channel flow.

1.1. *Localized disturbance in Newtonian channel flow*

Linear stability theory predicts that Poiseuille flow is stable up to a critical Reynolds number $Re = 3848$ based on the channel half-height and the bulk velocity (Orszag 1971). By appealing to Squire's theorem, at this critical Reynolds number the flow is unstable to a two-dimensional disturbance. Below the critical Reynolds number, while the flow does not possess any long-time instabilities, it can sustain transient energy amplification due to two- and three-dimensional disturbances of finite amplitude. Several growth mechanisms have been proposed for subcritical transition (Bayly, Orszag & Herbert 1988), and breakdown to turbulence in this regime is known as bypass transition (Orszag & Kells 1980): it bypasses the amplification of discrete instability waves seen in the natural transition route.

The evolution of a three-dimensional localized disturbance in channel flow has been studied by Henningson *et al.* (1993). According to those authors, a disturbance of small amplitude undergoes linear growth due to the lift-up mechanism (Landahl 1975) during which the three-dimensionality of the disturbance causes a growth in the wall-normal perturbation vorticity. The disturbance is dominated by the streamwise velocity component, and starts to become elongated in the streamwise direction. However, the period of energy amplification is short lived and the flow returns to a laminar state due to viscous dissipation. For disturbances with larger initial amplitude, nonlinearity transfers energy from the initially localized disturbance into lower streamwise wavenumbers. Elongated vortices are formed close to the wall and are further intensified by the mean shear. These elongated structures are most effective at generating streaks via the lift-up mechanism; the streaks themselves are dominated by high streamwise velocity fluctuations. The flow ultimately breaks down due to a roll-up process of the stretched vortical structures which is initiated due to sharp wall-normal gradients of streamwise velocity fluctuations. This process leads to a rapid growth of the wall-normal perturbation velocity and the formation of turbulent spots, as observed in experiments (Henningson & Andersson 1987) and in numerical simulations (Henningson & Kim 1991). After the inception of the spot, turbulence continues to spread and ultimately fills the entire channel.

The above description of transition follows a general classification into an initial linear stage, a secondary instability mechanism and ultimately a nonlinear spot inception. These general stages have been examined in various flow configurations and for transition due to different initial conditions. The early linear stage in subcritical transition is often attributed to non-modal energy amplification, for example due to the Orr mechanism for two-dimensional disturbances or lift-up for three-dimensional perturbations. In supercritical flows, the same mechanisms persist, but discrete instability waves can also play an important role in the linear stage. The second stage has been examined using secondary instability analyses, and the final stage where turbulent spots are formed is often examined empirically due to its nonlinear nature. Similarities in the transition process in different shear flows, and starting from various initial conditions, have emerged since they are related to the same fundamental mechanisms. In addition, transition due to localized initial disturbances in channel flow has been considered an informative testbed for the study of bypass transition (Henningson *et al.* 1993).

https://doi.org/10.1017/jfm.2014.586 Published online by Cambridge University Press

1.2. *Simulations of non-Newtonian channel flow*

The literature on viscoelastic channel flow has focused on the phenomenon of drag reduction in the fully turbulent regime upon the addition of polymers. DNS have been extensively employed to investigate this phenomenon and to evaluate the effects of viscoelasticity on turbulence (Sureshkumar, Beris & Handler 1997; Dimitropoulos, Sureshkumar & Beris 1998; Min, Yoo & Choi 2001; De Angelis, Casciola & Piva 2002; Dubief *et al.* 2005; Dallas, Vassilicos & Hewitt 2010; Tsukahara *et al.* 2011). DNS have also been used to isolate flow structures in minimal-flow-unit configurations: the smallest flow domain in which turbulence can be sustained (Stone, Waleffe & Graham 2002; Xi & Graham 2010). These efforts have revealed changes in the flow energetics, in particular the root-mean-square (r.m.s.) of the velocity fluctuations, and in the turbulence kinetic energy budget, which are in agreement with experimental measurements of surfactant-laden turbulent flow (Yu, Li & Kawaguchi 2004). A common observation in drag-reduced non-Newtonian turbulent flow is the decrease in the wall-normal and spanwise velocity perturbations (White & Mungal 2008), which is consistent with the observations of Xi & Graham (2012) who state that polymers weaken streamwise vortices. Connections between these changes and the mechanism for the sustenance of a drag-reduced state have been suggested (e.g. Min *et al.* 2003*b*; Dubief *et al.* 2004). However, despite the extensive experiments and numerical records of the effects of viscoelasticity on the flow, the mechanisms through which polymer chains cause these changes have not been fully isolated due to the complex nature of fully turbulent flow.

Unlike simulations of fully turbulent channel flow, nonlinear simulations of transition in this flow configuration are absent from the literature. The study of transition, however, provides a unique manner to examine the changes to the flow in both the linear stages and in the nonlinear regime due to polymeric effects. In the latter regime, changes to isolated flow structures become evident, unlike the more complex fully turbulent configuration. The existing literature on transition in bounded polymeric shear flows is primarily focused on the linear regime, which has been examined using linear stability theory. The effect of Reynolds number and elasticity on energy amplification of channel flows of Oldroyd-B fluid was studied by Hoda, Jovanovic & Kumar (2008, 2009), while Page & Zaki (2014) have analysed streak amplification in Oldroyd-B Couette flow. Zhang *et al.* (2013) report the effects of viscoelasticity on oblique modes in a channel flow of finitely extensible nonlinear elastic fluid with the Peterlin closure (FENE-P), which is relevant to the current study. Numerical simulations of the entire transition process would therefore complement these studies, and are performed herein. Starting from an initially localized disturbance, transition to turbulence in a polymeric channel flow is simulated and analysed in detail. The governing equations and a description of the simulation setup are presented in § 2. Results from the linear evolution regime are discussed in § 3, followed by a discussion of the results from the nonlinear regime in § 4. Finally, concluding remarks are provided in § 5.

2. Governing equations and simulation set-up

Assuming a uniform concentration of the polymeric solution, the incompressible Navier–Stokes equations for viscoelastic flow take the form,

$$\frac{\partial u_i}{\partial t} + u_j \frac{\partial u_i}{\partial x_j} = -\frac{\partial p}{\partial x_i} + \frac{\beta}{Re} \frac{\partial^2 u_i}{\partial x_j^2} + \frac{1-\beta}{Re} \frac{\partial \tau_{ij}}{\partial x_j} \tag{2.1}$$

https://doi.org/10.1017/jfm.2014.586 Published online by Cambridge University Press

$$\frac{\partial u_i}{\partial x_i} = 0. \tag{2.2}$$

In these equations, $\beta \in [0, 1]$ is the ratio of the solvent to the total viscosity and is effectively a measure of the polymer concentration. The polymeric stress, τ_{ij}, accounts for the interaction between the solvent and the polymer, and depends on the extension of the polymer chains which is represented by the conformation tensor, c_{ij}. This tensor is the ensemble average $\langle q_i q_j \rangle$, where q_i is the end-to-end vector of a polymer molecule. The polymer stress, τ_{ij}, is obtained from the polymer conformation tensor according to the FENE-P model,

$$\tau_{ij} = \frac{1}{We}\left(\frac{c_{ij}}{\psi} - \frac{\delta_{ij}}{a}\right) \tag{2.3}$$

$$\psi = 1 - \frac{c_{kk}}{L_{max}^2} \tag{2.4}$$

$$a = 1 - \frac{3}{L_{max}^2}. \tag{2.5}$$

The Weissenberg number, *We*, is the ratio of the polymer relaxation and the flow time scales. The maximum dimensionless extensibility of the polymer chain is L_{max}. Finally, the conformation tensor satisfies the evolution equation,

$$\frac{\partial c_{ij}}{\partial t} + u_k \frac{\partial c_{ij}}{\partial x_k} = c_{kj}\frac{\partial u_i}{\partial x_k} + c_{ik}\frac{\partial u_j}{\partial x_k} - \tau_{ij}, \tag{2.6}$$

which includes advection by the velocity field, stretching due to the strain exerted on the polymer chains, and relaxation due to the elastic nature of the polymer.

The accuracy of the FENE-P model in predicting polymeric stresses has been studied extensively by Zhou & Akhavan (2003) who compared results for the pre-averaged models with those for the FENE chain. The FENE-P model was found to over-predict the polymeric stresses in elongational and shear flows, which results in numerical inaccuracies especially in regions of strong polymer stretching. However, the FENE-P results are found to be in qualitative agreement with those for the FENE chain. As a result, after addressing any numerical instabilities through appropriate computational methods, the model has been used extensively to simulate non-Newtonian channel flow (Dimitropoulos *et al.* 1998; Dubief *et al.* 2004; Dallas *et al.* 2010).

Simulations of non-Newtonian flows are challenging due to the hyperbolic nature of the conformation tensor evolution equation (El-Kareh & Leal 1989). For example, sharp gradients form in the conformation field and can lead to numerical instabilities and errors. Several measures have been suggested in the literature in order to ensure stability and accuracy. For example, Sureshkumar & Beris (1995) state that upwind schemes along with artificial diffusivity increase the stability of the numerical solution of hyperbolic equations. Vaithianathan & Collins (2003) note that, in simulations of polymeric fluids with a maximum extensibility constraint, numerical errors can lead to predictions of the polymer extension that exceed their bounds. This problem can be resolved by evaluating the conformation tensor equation implicitly.

The numerical method for the solution of the governing equations follows the general approach by Min, Yoo & Choi (2003*a*). The spatial discretization of the Navier–Stokes equations is performed using a control-volume formulation. The

https://doi.org/10.1017/jfm.2014.586 Published online by Cambridge University Press

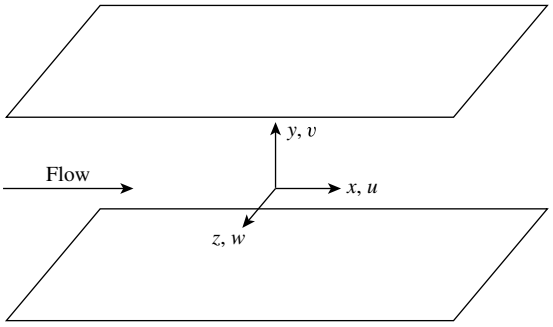


FIGURE 1. Flow configuration and coordinate system.

equation is advanced in time using a fractional-step algorithm where diffusion and polymer stress terms are treated implicitly using Crank–Nicholson, and the advection term is treated explicitly. Spatial derivatives of the conformation tensor in (2.6) are computed using a third-order upwind central scheme. To ensure numerical stability, a local artificial diffusivity is added at locations where the conformation tensor loses its positive definiteness (Min *et al.* 2001). This additional term takes the form $\kappa \Delta_k^2(\partial^2 c_{ij}/\partial x_k^2)$, where Δ_k is the local grid spacing in the k direction (Dubief *et al.* 2005). The coefficient κ is set to 10^{-3} for all simulations. This value is sufficiently small, and guarantees that artificial diffusivity is inactive in the linear evolution, and is restricted to less than 10 % of the grid nodes during transition, which is consistent with the recommendation by Dubief *et al.* (2005).

The flow configuration is shown in figure 1. Periodic boundary conditions are enforced in the streamwise, x, and spanwise, z, directions and no-slip conditions at both walls. The simulations are performed at a Reynolds number $Re = 2000$ based on the channel half-height, h, and the bulk flow velocity, U_b. The Weissenberg number is therefore $We \equiv \lambda U_b/h$, where λ is the polymer relaxation time. Throughout this work, time, t, is normalized by the convective time scale, h/U_b, but can readily be expressed in reference to the relaxation time scale, $t_\lambda = t/We$.

The mass flow rate is maintained constant by adjusting the required streamwise pressure gradient. Since the focus is on bypass transition, the Reynolds number is lower than the critical value for Newtonian channel flow, $Re_c = 3848$ (Orszag 1971), and non-Newtonian flow at similar rheological conditions, $Re_c = 3600$ for a FENE-P fluid at $\beta = 0.9$ and high maximum extensibility (see figure 5 in Zhang *et al.* 2013).

The initial condition for the simulations consists of a laminar base state, along with a localized velocity perturbation. The laminar base state for non-Newtonian flow, as reported by Richter, Iaccarino & Shaqfeh (2010), is given by

$$U(y) = \frac{Re}{2\beta}\frac{\mathrm{d}P}{\mathrm{d}x}(y^2-1) - \frac{1-\beta}{\beta}\frac{3}{8J_0}\left[(F^+(y)G^-(y) + F^-(y)G^+(y)) - (F^+(h)G^-(h) + F^-(h)G^+(h))\right] \tag{2.7}$$

$$F^\pm(y) = \left(J_0 y \pm \sqrt{(J_0 y)^2 + K_0^3}\right)^{1/3} \tag{2.8}$$

$$G^\pm(y) = \left(3J_0 y \pm \sqrt{(J_0 y)^2 + K_0^3}\right)^{1/3} \tag{2.9}$$

https://doi.org/10.1017/jfm.2014.586 Published online by Cambridge University Press

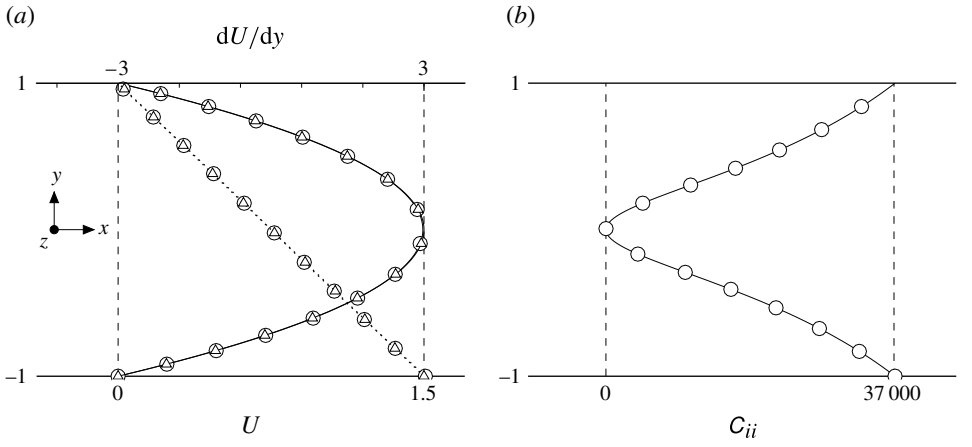


FIGURE 2. Mean velocity profile, mean shear, and trace of the conformation tensor at $t = 0$ for $Re = 2000$: · · · ·, $\mathrm{d}U/\mathrm{d}y$; △, Newtonian flow; ○, non-Newtonian flow at $We = 100$, $L_{max} = 300$ and $\beta = 0.9$.

$$J_0 = \frac{Re}{4\beta}\left(\frac{L_{max}}{aWe}\right)^2 \frac{\mathrm{d}P}{\mathrm{d}x} \tag{2.10}$$

$$K_0 = \frac{1}{6\beta}\left(\frac{L_{max}}{aWe}\right)^2. \tag{2.11}$$

The difference between the velocity profiles for Poiseuille ($\beta = 1$ in (2.7)) and non-Newtonian laminar flow is negligible for the values of We and β used here as demonstrated by the comparison in figure 2. The trace of the associated polymeric conformation tensor is also shown.

The localized disturbance added to the base flow is a pair of counter-rotating vortices (figure 3), previously used by Henningson *et al.* (1993) in simulations of Newtonian channel flow. The disturbance is placed at the centre of the channel and spans the entire channel height. The streamwise and spanwise extents, and the disturbance orientation and amplitude can be specified. The disturbance streamfunction and velocity are

$$\psi = \epsilon f(y)\left(\frac{x'}{l_x}\right) z' \exp\left[-\left(\frac{x'}{l_x}\right)^2 - \left(\frac{z'}{l_z}\right)^2\right] \tag{2.12}$$

$$(u', v', w') = \left(-\frac{\partial\psi}{\partial y}\sin\theta, \frac{\partial\psi}{\partial z'}, -\frac{\partial\psi}{\partial y}\cos\theta\right) \tag{2.13}$$

$$(x', z') = (x\cos\theta - z\sin\theta, x\sin\theta + z\cos\theta) \tag{2.14}$$

$$f(y) = (1+y)^p(1-y)^q. \tag{2.15}$$

The constants l_x, l_y and l_z are the streamwise, wall-normal and spanwise length scales of the disturbance and ϵ is its amplitude. For this study, $l_x = l_z = 2$. The exponents of the wall-normal dependence are also equal, $p = q = 2$. The orientation of the disturbance in the horizontal plane is dependent on θ; for the current study, $\theta = 0$.

Details of the parameters of the computational domain are provided in table 1. The dimensions are in accordance with the recommendation by Li, Sureshkumar &

https://doi.org/10.1017/jfm.2014.586 Published online by Cambridge University Press

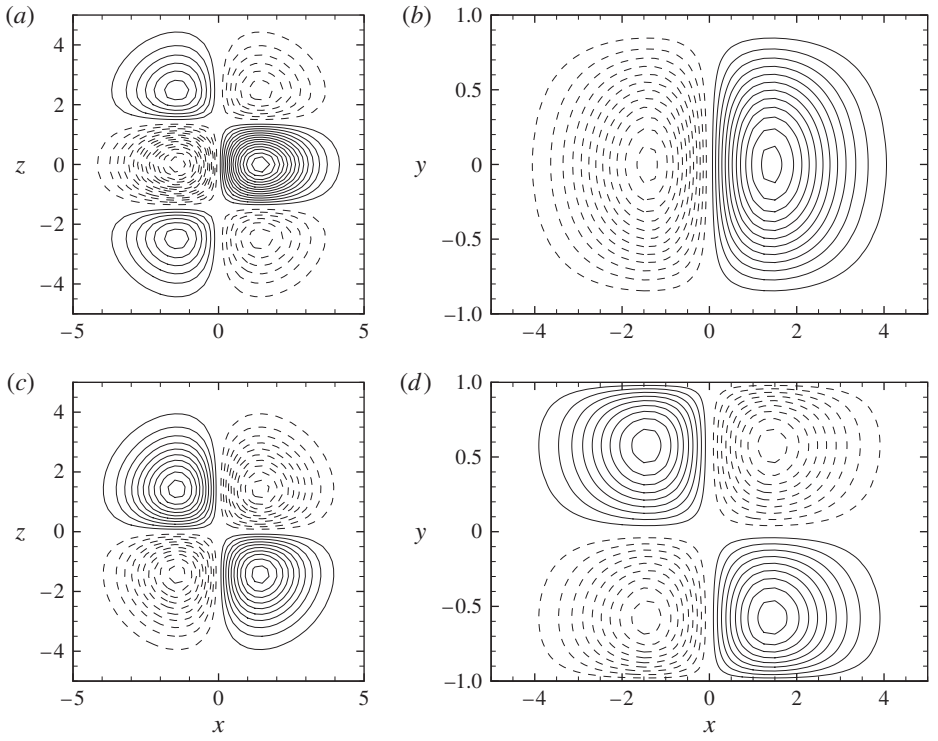


FIGURE 3. Initial wall-normal and spanwise velocity perturbation fields: (*a*) v' at $y = -0.56$, contour spacing 2.0×10^{-6}; (*b*) v' at $z = -1.0$, contour spacing 2.0×10^{-6}; (*c*) w' at $y = -0.56$, contour spacing 8.0×10^{-6}; (*d*) w' at $z = -1.0$, contour spacing 8.0×10^{-6}. Solid and dashed lines indicate positive and negative velocities, respectively.

Khomami (2006) for fully turbulent non-Newtonian flow. The grid spacing is uniform in the streamwise and spanwise directions and is given by a hyperbolic tangent stretching in the wall-normal coordinate. A grid refinement study was performed in order to ensure that the flow in the Newtonian and non-Newtonian cases is fully resolved.

In the following, instantaneous flow variables are decomposed according to $\phi(\boldsymbol{x}, t) = \overline{\phi}(y, t) + \phi'(\boldsymbol{x}, t)$. Overline and uppercase denote variables that are averaged in both the streamwise and spanwise directions, and $\phi'(\boldsymbol{x}, t)$ is the perturbation. Where integral quantities are plotted, they are averaged over the bottom half of the channel and are defined as, $\widehat{\phi}(t) \equiv 1/(L_y/2) \int_{-L_y/2}^{0} \overline{\phi}(y, t)\mathrm{d}y$. The difference between the non-Newtonian and Newtonian ($\widehat{\phi}_N(t)$) values of a quantity is denoted by $[\widehat{\phi}](t) = \widehat{\phi}(t) - \widehat{\phi}_N(t)$.

3. Evolution of linear disturbance

The study of transition is often aided by considering the evolution of small-amplitude, or linear, perturbations. In order to examine linear effects, a vortex pair with an amplitude $\epsilon = 1.5 \times 10^{-4}$ is prescribed as the initial disturbance. In the Orr–Sommerfeld and Squire equations for the wall-normal velocity and vorticity, the three-dimensionality of the initial disturbance, namely $\partial v'/\partial z$, causes forcing of the wall-normal vorticity perturbation. This results in an increase in the

https://doi.org/10.1017/jfm.2014.586 Published online by Cambridge University Press

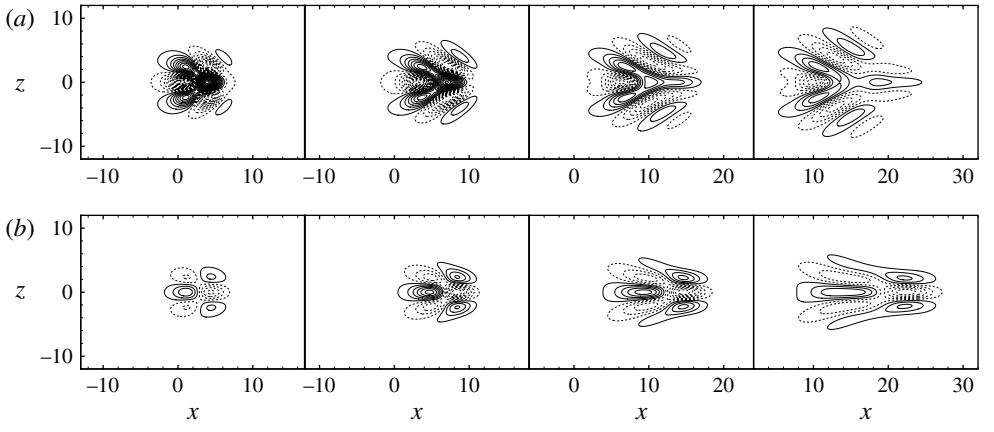


FIGURE 4. Evolution of the disturbance ($\epsilon = 1.5 \times 10^{-4}$) in Newtonian flow at $y = -0.56$ and $t = \{3, 7, 13, 20\}$. Contours denote (*a*) wall-normal v' and (*b*) streamwise u' velocity perturbations.

Disturbance amplitude (ϵ)	Computational grid ($N_x \times N_y \times N_z$)	Grid resolution ($\Delta_x^+ \times \Delta_{y,min}^+ \times \Delta_z^+$)
0.00015	$384 \times 320 \times 384$	—
0.10485	$384 \times 320 \times 384$	—
0.20970	$1024 \times 400 \times 512$	$6.19 \times 0.03 \times 6.19$

TABLE 1. Parameters describing the computational domain and grid. The computational domain for all simulations presented has dimensions $L_x = 48$, $L_y = 2$, $L_z = 24$. The grid resolution is normalized by the wall variable $y^+ = yu_\tau/\nu$ where ν is the kinematic viscosity and u_τ the friction velocity in the fully turbulent Newtonian flow.

streamwise velocity perturbation and therefore energy growth owing to the linear lift-up mechanism (figure 4). This growth is opposed and eventually damped by viscous dissipation. Snapshots of the disturbance in Newtonian flow (figure 4) show the effect of dissipation: a decrease in the magnitude of perturbation velocities is observed at large times during the disturbance evolution. In figure 5, the evolution of the disturbance energy per unit volume, $E(t)$, is plotted and is normalized by its initial value E_0,

$$E(t) \equiv \frac{1}{L_x \times L_z \times L_y/2} \int_{-L_y/2}^{0} \int_{-L_z/2}^{L_z/2} \int_{-L_x/2}^{L_x/2} \frac{1}{2}(u'^2 + v'^2 + w'^2) \mathrm{d}x\mathrm{d}z\mathrm{d}y. \tag{3.1}$$

The same trend of energy growth and decay in Newtonian flow is followed in the non-Newtonian case (figure 5*a*), but the extent of energy amplification decreases. For the non-Newtonian cases shown, the energy suppression varies from approximately 5 to 15 %, depending on the elasticity of the flow. A decomposition of the perturbation energy in the three coordinate directions is shown in figure 5(*b*). The wall-normal and spanwise energy make up a progressively smaller fraction of the total energy with time. The streamwise energy, on the other hand, becomes dominant for $t > 3.28$. Its amplification and further decay therefore dictate the shape of the $E(t)$ curve in

https://doi.org/10.1017/jfm.2014.586 Published online by Cambridge University Press

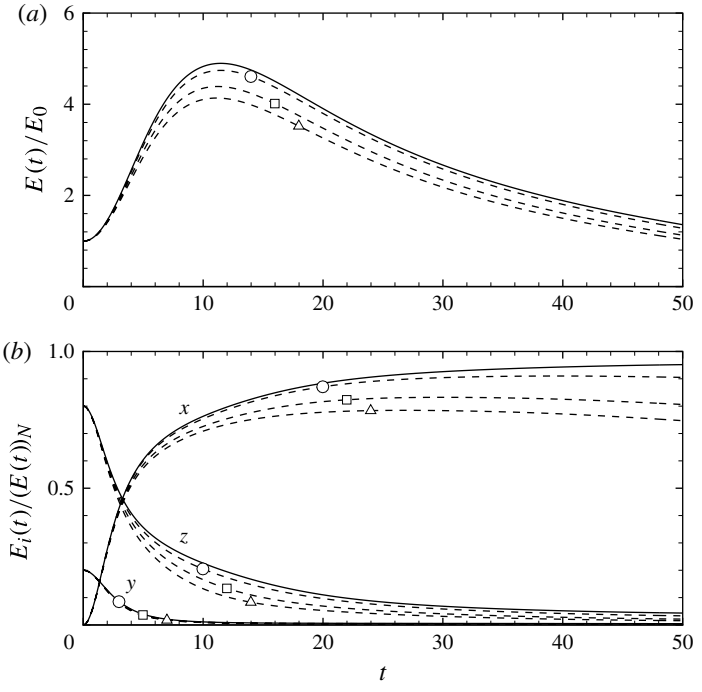


FIGURE 5. Evolution of perturbation energy for $\epsilon = 1.5 \times 10^{-4}$. (*a*) Amplification of total perturbation energy normalized by the initial value. (*b*) Components of perturbation energy, $E_i(t)$, normalized by the total energy in the Newtonian flow, $(E(t))_N$. ——, Newtonian flow; - - - -, non-Newtonian flow at $L_{max} = 300$ and $\beta = 0.9$; ○, $We = 15$; □, $We = 40$; △, $We = 100$.

figure 5(*a*). Relative to the Newtonian case, viscoelasticity causes a faster decay in the spanwise energy and suppresses the streamwise energy growth. During the initial phase of energy amplification, these two components are comparable in magnitude. The wall-normal component is also suppressed, although inappreciably.

We now examine the influence of the ratio We/L_{max} on $E_{max} \equiv \max_t\{E(t)\}$, shown in figure 6, where the maximum perturbation kinetic energy is normalized by the Newtonian value, $E_{max,N}$. For low We/L_{max}, viscoelasticity appears to enhance transient growth, although inappreciably. The main region of interest here is for higher We/L_{max}, where a significant decrease in the maximum perturbation energy is observed. This trend is consistent with the optimal disturbance results by Zhang *et al.* (2013). Those authors reported a stabilizing effect of oblique disturbances at high *We*. The origin of the stabilizing influence observed in figure 6 is analysed in the next section by examining the perturbation-energy equation. The case with $We = 40$ and $L_{max} = 300$ is examined in detail since this relatively high Weissenberg number emphasizes the difference between the Newtonian and non-Newtonian flow. The change in trend at $We/L_{max} \sim 0.5$ is explained in § 3.2.

An energy analysis was also performed by Hoda *et al.* (2009) for a non-Newtonian channel flow perturbed with stochastic body forcing. In order to isolate the mechanism for streak formation and amplification, they focused on streamwise-independent linear disturbances. In contrast, the localized disturbance in the current study has a finite

https://doi.org/10.1017/jfm.2014.586 Published online by Cambridge University Press

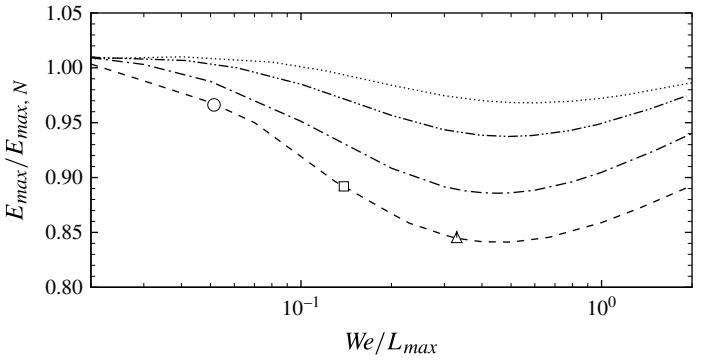


FIGURE 6. The effect of elasticity on the maximum perturbation energy in non-Newtonian flow: ····, $L_{max} = 50$; — · · —, $L_{max} = 100$; — · —, $L_{max} = 200$; - - - -, $L_{max} = 300$; ○, $We = 15$; □, $We = 40$; △, $We = 100$.

streamwise and spanwise extent, and the associated terms play an important role in the energy evolution.

3.1. *Energy analysis*

For the non-Newtonian polymeric flow, the transport equation for the Reynolds stress is given by

$$\begin{aligned}\frac{\partial \overline{u_i' u_j'}}{\partial t} = & \underbrace{-U_k \frac{\partial \overline{u_i' u_j'}}{\partial x_k}}_{\mathscr{A}_{ij}} \underbrace{-\frac{\partial \overline{u_i' u_j' u_k'}}{\partial x_k}}_{\mathscr{Q}_{ij}} \underbrace{-\left(\overline{u_j' \frac{\partial p'}{\partial x_i}} + \overline{u_i' \frac{\partial p'}{\partial x_j}}\right)}_{\phi_{ij}} \\ & \underbrace{-\left(\overline{u_j' u_k'} \frac{\partial U_i}{\partial x_k} + \overline{u_i' u_k'} \frac{\partial U_j}{\partial x_k}\right)}_{\mathscr{P}_{ij}} + \underbrace{\frac{\beta}{Re} \frac{\partial^2 \overline{u_i' u_j'}}{\partial x_k^2}}_{\mathscr{D}_{ij}} \\ & \underbrace{-2\frac{\beta}{Re} \overline{\frac{\partial u_i'}{\partial x_k} \frac{\partial u_j'}{\partial x_k}}}_{\epsilon_{ij}} + \underbrace{\frac{1-\beta}{Re} \left(\overline{u_j' \frac{\partial \tau_{ik}'}{\partial x_k}} + \overline{u_i' \frac{\partial \tau_{jk}'}{\partial x_k}}\right)}_{\mathscr{W}_{ij}}. \end{aligned} \tag{3.2}$$

The evolution equation for the perturbation energy is obtained by setting $i = j$,

$$\frac{1}{2} \frac{\partial \widehat{u_i' u_i'}}{\partial t} = \frac{\partial E}{\partial t} = \frac{1}{2} (\widehat{\mathscr{A}_{ii}} + \widehat{\mathscr{Q}_{ii}} + \widehat{\phi_{ii}} + \widehat{\mathscr{P}_{ii}} + \widehat{\mathscr{D}_{ii}} + \widehat{\epsilon_{ii}} + \widehat{\mathscr{W}_{ii}}). \tag{3.3}$$

In the above equation, repeating indices imply summation over the three coordinate directions. In (3.2), $\mathscr{A}_{ij}$ is mean advection, $\mathscr{Q}_{ij}$ is energy transport by fluctuations, ϕ_{ij} is pressure redistribution, $\mathscr{P}_{ij}$ is production, $\mathscr{D}_{ij}$ is viscous diffusion, ϵ_{ij} is dissipation and $\mathscr{W}_{ij}$ is polymer work. The polymer work, $\mathscr{W}_{ij}$, depends on the perturbation to the polymer stress. The latter is governed by the evolution equation for the perturbation to the conformation tensor,

https://doi.org/10.1017/jfm.2014.586 Published online by Cambridge University Press

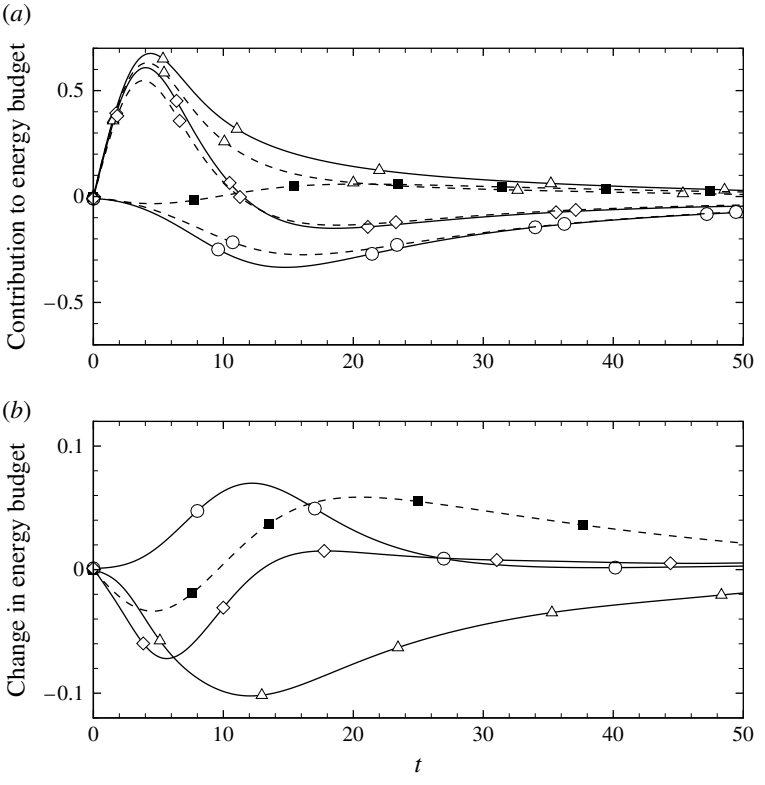


FIGURE 7. Components of the perturbation energy budget (see (3.3)): (*a*) ——, Newtonian flow; - - - -, non-Newtonian flow at $L_{max} = 300$, $\beta = 0.9$, $We = 40$; △, $\widehat{\mathscr{P}_{ii}}/2E_0$; ○, $\widehat{\epsilon_{ii}}/2E_0$; ■, $\widehat{\mathscr{W}_{ii}}/2E_0$; ◇, $(1/2E_0)\partial\widehat{u_i'u_i'}/\partial t$; (*b*) △, $[\widehat{\mathscr{P}_{ii}}/2E_0]$; ○, $[\widehat{\epsilon_{ii}}/2E_0]$; ■, $\widehat{\mathscr{W}_{ii}}/2E_0$; ◇, $[(1/2E_0)\partial\widehat{u_i'u_i'}/\partial t]$.

$$\left(\frac{\partial}{\partial t} + U_k\frac{\partial}{\partial x_k}\right)c_{ij}' = -u_k'\frac{\partial C_{ij}}{\partial x_k} - u_k'\frac{\partial c_{ij}'}{\partial x_k} + C_{kj}\frac{\partial u_i'}{\partial x_k} + c_{kj}'\frac{\partial U_i}{\partial x_k} + c_{kj}'\frac{\partial u_i'}{\partial x_k} + C_{ik}\frac{\partial u_j'}{\partial x_k} + c_{ik}'\frac{\partial U_j}{\partial x_k} + c_{ik}'\frac{\partial u_j'}{\partial x_k} - \tau_{ij}'. \tag{3.4}$$

In the linear evolution, the production, dissipation and polymer work are the only significant contributors to the energy budget (3.3). These contributions are compared with the Newtonian reference simulation in figure 7(*a*) and the difference between the Newtonian and non-Newtonian simulations is plotted in figure 7(*b*). Relative to the Newtonian case, both the production and dissipation are reduced, and the difference between the energy growth rate in the non-Newtonian and Newtonian flows, $[\partial\widehat{u_i'u_i'}/\partial t]$, is negative thus signalling weaker energy amplification in the polymeric flow. The maximum $[\partial\widehat{u_i'u_i'}/\partial t]$ is recorded near $t \sim 6$ and is primarily due to a negative polymer work and a decrease in production, both of which contribute to the weaker energy amplification in the flow. The decrease in production is in agreement with the observations of Dimitropoulos *et al.* (1998) and Zhang *et al.* (2013) and represents a weaker rate of energy transfer from the mean flow to velocity fluctuations. The

https://doi.org/10.1017/jfm.2014.586 Published online by Cambridge University Press

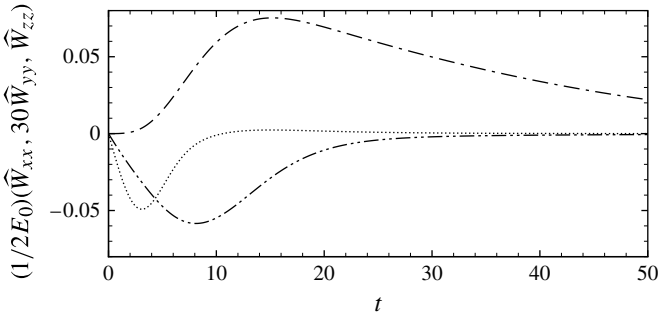


FIGURE 8. Evolution of the components of polymer work for $We = 40$, $L_{max} = 300$ and $\beta = 0.9$; — · —, $\widehat{\mathscr{W}_{xx}}/2E_0$; · · · ·, $30\widehat{\mathscr{W}_{yy}}/2E_0$; — · · —, $\widehat{\mathscr{W}_{zz}}/2E_0$.

negative polymer work indicates that energy from the velocity fluctuations is exerted as work onto the polymer chains, an assertion which is further examined below.

3.1.1. *Polymer work*

Since the initial disturbance is a streamwise vortex with the majority of the energy in the spanwise component (see figure 5*b*), the polymer work term is expected to affect primarily the spanwise component of the velocity disturbance at early time. This view is supported by figure 8 where the time evolution of the polymer work is reported. The wall-normal polymer work is multiplied by a factor of 30 in the figure to emphasize that it is slightly negative. While this component is smaller than the dominant spanwise polymer work, it has an indirect effect on energy which will be analysed in the next section. Most relevant here, however, is the negative $\widehat{\mathscr{W}_{zz}}$ at early time,

$$\begin{aligned}\mathscr{W}_{zz} &= \frac{2(1-\beta)}{Re}\left(\overline{w'\frac{\partial \tau'_{xz}}{\partial x}} + \overline{w'\frac{\partial \tau'_{yz}}{\partial y}} + \overline{w'\frac{\partial \tau'_{zz}}{\partial z}}\right)\\ &= \mathscr{W}_{zz(x)} + \mathscr{W}_{zz(y)} + \mathscr{W}_{zz(z)}.\end{aligned} \tag{3.5}$$

The relation between polymeric stress and conformation tensor is given by (2.3). An expression for the polymeric stress perturbation is derived by simplifying the equation using a Taylor series expansion and taking into account that $C_{kk} + c'_{kk} < L^2_{max}$ for the set of non-Newtonian parameters ($We \sim O(10)$, $L_{max} \sim O(10^2)$) used in this study,

$$\tau'_{ij} \approx \frac{1}{We}\left(\frac{C_{ij}c'_{kk}}{L^2_{max}} + c'_{ij}\left(1 + \frac{C_{kk} + c'_{kk}}{L^2_{max}}\right)\right) \approx \left(1 + \frac{C_{kk}}{L^2_{max}}\right)\frac{c'_{ij}}{We}. \tag{3.6}$$

The final simplification in the equation above is valid for $C_{ij}/L^2_{max} \ll 1$. This holds for all components except $i = j = x$ since $C_{xx} \sim O(We^2)$. In order to explain the origin of the spanwise polymer work, we consider the evolution of a small-amplitude perturbation to the conformation tensor governed by the linear approximation of the full transport equation for the conformation tensor perturbation (3.4),

$$\left(\frac{\partial}{\partial t} + U_k\frac{\partial}{\partial x_k}\right)c'_{ij} = -u'_k\frac{\partial C_{ij}}{\partial x_k} + C_{kj}\frac{\partial u'_i}{\partial x_k} + c'_{kj}\frac{\partial U_i}{\partial x_k} + C_{ik}\frac{\partial u'_j}{\partial x_k} + c'_{ik}\frac{\partial U_j}{\partial x_k} - \tau'_{ij}. \tag{3.7}$$

https://doi.org/10.1017/jfm.2014.586 Published online by Cambridge University Press

For the current mean flow, $V = W = 0$ and $C_{xz} = C_{yz} = 0$. Therefore, the conformation tensor perturbations obey the governing equations,

$$\left(\frac{\partial}{\partial t} + U\frac{\partial}{\partial x}\right) c'_{xz} = C_{zz}\frac{\partial u'}{\partial z} + c'_{yz}\frac{\partial U}{\partial y} + C_{xx}\frac{\partial w'}{\partial x} + C_{xy}\frac{\partial w'}{\partial y} - \tau'_{xz}$$
$$\approx \underbrace{\frac{\partial w'}{\partial x} C_{xx}}_{o\left(\frac{w'}{l_x} We^2\right)} \tag{3.8}$$

$$\left(\frac{\partial}{\partial t} + U\frac{\partial}{\partial x}\right) c'_{yz} = C_{zz}\frac{\partial v'}{\partial z} + C_{xy}\frac{\partial w'}{\partial x} + C_{yy}\frac{\partial w'}{\partial y} - \tau'_{yz}$$
$$\approx \underbrace{\frac{\partial w'}{\partial x} C_{xy}}_{o\left(\frac{w'}{l_x} We\right)} \tag{3.9}$$

$$\left(\frac{\partial}{\partial t} + U\frac{\partial}{\partial x}\right) c'_{zz} = -v'\frac{\partial C_{zz}}{\partial y} + 2C_{zz}\frac{\partial w'}{\partial z} - \tau'_{zz}$$
$$\approx \underbrace{-v'\frac{\partial C_{zz}}{\partial y}}_{o\left(\frac{v'}{l_y}\right)} + \underbrace{2C_{zz}\frac{\partial w'}{\partial z}}_{o\left(\frac{w'}{l_z}\right)}. \tag{3.10}$$

The above approximations are valid at short time ($t < We$) and take into account that $C_{zz} \sim O(1)$, $C_{xy} \sim O(We)$ and $C_{xx} \sim O(We^2)$. Further, the extent of the disturbance in all three directions (l_x, l_y, l_z) is comparable at the early time. From the above equations, it is evident that the perturbation c'_{xz}, and in turn τ'_{xz}, are dominant contributors to the negative spanwise polymer work. The physical mechanism in the approximation (3.8) is the action of the initial wall-normal vorticity which tilts, or rotates, the mean C_{xx} component of the conformation tensor and thus creates a perturbation c'_{xz}. This will in turn result in the polymer stress perturbation τ'_{xz}, and ultimately a negative polymer work term $\overline{w'(\partial\tau'_{xz}/\partial x)}$ in the $\overline{w'w'}$ equation. Therefore, the kinetic energy from the spanwise velocity perturbation field is diminished as it is expended to stretch the polymer chains in the x–z plane. Contour plots from the simulation at $t = 4$ support this view: in figure 9(*a*), $\partial w'/\partial x$ is in phase with c'_{xz}, consistent with the approximation (3.8). Furthermore, the resulting negative polymer work, $\mathscr{W}_{zz(x)}$, is captured by the negative correlation between w' and $\partial\tau'_{xz}/\partial x$ in figure 9(*b*). In summary, the wall-normal vorticity triggers a resistive spanwise polymer work which weakens the spanwise velocity of the localized disturbance as shown by the energy curves in figure 5(*b*).

3.1.2. *Production of disturbance kinetic energy*

When considering the variation in the production term relative to Newtonian flow in figure 7, it is important to note that the change in the mean-velocity profile is negligible when the disturbance evolution is linear. Therefore the change in the averaged shear stress, $-\overline{u'v'}$, is responsible for the decrease in production. The shear stress is, in turn, weaker due to a decrease in its own production term, $\overline{v'v'}(\partial U/\partial y)$, during the initial energy growth phase (see figure 10).

https://doi.org/10.1017/jfm.2014.586 Published online by Cambridge University Press

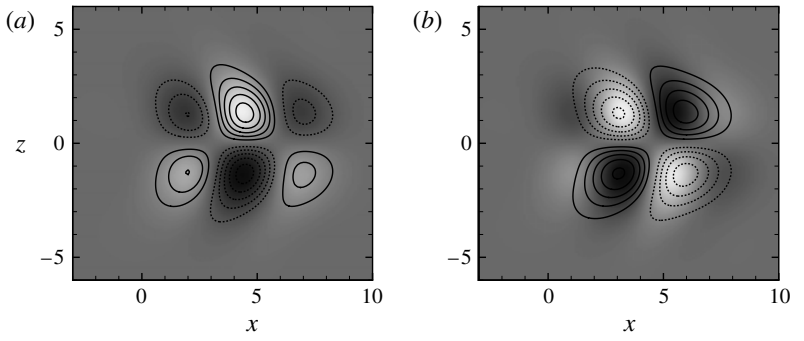


FIGURE 9. Snapshots at $t = 4$, $y = -0.56$ during the evolution of the small-amplitude vortex pair in non-Newtonian flow at $We = 40$, $L_{max} = 300$ and $\beta = 0.9$. (*a*) Contour lines, $\partial w'/\partial x$ (contour spacing 2×10^{-5}); flood, c'_{xz} (contour range $[-3, 3]$). (*b*) Contour lines, w' (contour spacing 2×10^{-5}); flood, $\partial \tau'_{xz}/\partial x$ (contour range $[-8 \times 10^{-2}, 8 \times 10^{-2}]$).

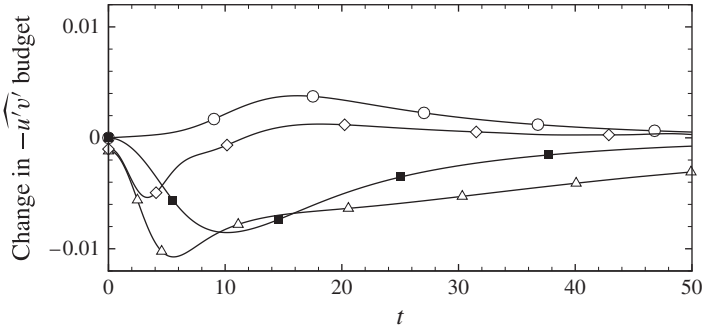


FIGURE 10. Difference between the corresponding components of the shear stress budget in non-Newtonian and Newtonian flow: △, $[-\widehat{\mathscr{P}}_{xy}/2E_0]$; ○, $[-\widehat{\epsilon}_{xy}/2E_0]$; ■, $-\widehat{\mathscr{W}}_{xy}/2E_0$; ◇, $[-(1/2E_0)\partial\widehat{u'v'}/\partial t]$.

The reduction in $\overline{v'v'}$ is examined by computing its budget (figure 11). The results demonstrate that the decrease in $\overline{v'v'}$ is mainly caused by a negative wall-normal polymer work,

$$\begin{aligned} \mathscr{W}_{yy} &= \frac{2(1-\beta)}{Re}\left(\overline{v'\frac{\partial \tau'_{xy}}{\partial x}} + \overline{v'\frac{\partial \tau'_{yy}}{\partial y}} + \overline{v'\frac{\partial \tau'_{zy}}{\partial z}}\right) \\ &= \mathscr{W}_{yy(x)} + \mathscr{W}_{yy(y)} + \mathscr{W}_{yy(z)}. \end{aligned} \tag{3.11}$$

The origin of this component of the polymer work can be explained in a manner similar to that for the negative spanwise polymer work. Taking into account the simplification for the polymeric stress perturbation in (3.6) and the base state ($V = W = 0$ and $C_{xz} = C_{yz} = 0$), the evolution of the relevant conformation tensor perturbations is determined from (3.7),

https://doi.org/10.1017/jfm.2014.586 Published online by Cambridge University Press

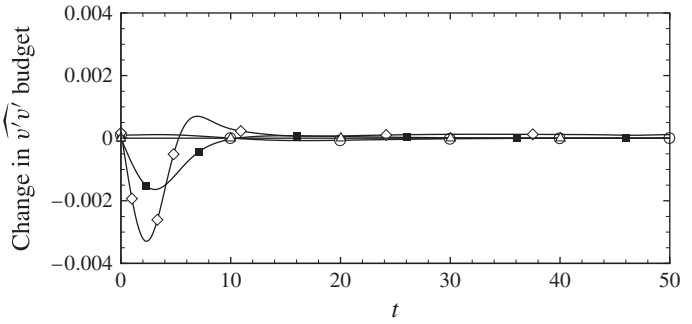


FIGURE 11. Difference between the corresponding components of $\partial\overline{v'^2}/\partial t$ (see (3.2)) in non-Newtonian and Newtonian flow: △, $[\widehat{\mathscr{P}}_{yy}/2E_0]$; ○, $[\widehat{\epsilon}_{yy}/2E_0]$; ■, $\widehat{\mathscr{W}}_{yy}/2E_0$; ◇, $[(1/2E_0)\partial\widehat{v'v'}/\partial t]$.

$$\left(\frac{\partial}{\partial t}+U\frac{\partial}{\partial x}\right)c'_{xy} = -v'\frac{\partial C_{xy}}{\partial y}+C_{xy}\frac{\partial u'}{\partial x}+C_{yy}\frac{\partial u'}{\partial y}+c'_{yy}\frac{\partial U}{\partial y} + C_{xx}\frac{\partial v'}{\partial x}+C_{xy}\frac{\partial v'}{\partial y}-\tau'_{xy} \approx \underbrace{\frac{\partial v'}{\partial x}C_{xx}}_{o\left(\frac{v'}{l_x}We^2\right)} \tag{3.12}$$

$$\left(\frac{\partial}{\partial t}+U\frac{\partial}{\partial x}\right)c'_{yy} = -v'\frac{\partial C_{yy}}{\partial y}+2\left(C_{xy}\frac{\partial v'}{\partial x}+C_{yy}\frac{\partial v'}{\partial y}\right)-\tau'_{yy} \approx \underbrace{2\frac{\partial v'}{\partial x}C_{xy}}_{o\left(\frac{v'}{l_x}We\right)} \tag{3.13}$$

$$\left(\frac{\partial}{\partial t}+U\frac{\partial}{\partial x}\right)c'_{yz} = C_{zz}\frac{\partial v'}{\partial z}+C_{xy}\frac{\partial w'}{\partial x}+C_{yy}\frac{\partial w'}{\partial y}-\tau'_{yz} \approx \underbrace{\frac{\partial w'}{\partial x}C_{xy}}_{o\left(\frac{w'}{l_x}We\right)}. \tag{3.14}$$

As for the spanwise polymer work, the approximations above are valid for early time and utilize the relations, $C_{xy}\sim O(We)$ and $C_{xx}\sim O(We^2)$. Comparing the simplified equations, c'_{xy} is the dominant contributor to the wall-normal polymer work. The approximation (3.12) is the action of the spanwise vorticity perturbation $\partial v'/\partial x$ which tilts, or rotates, the mean conformation tensor C_{xx}, and thus amplifies c'_{xy}. This is captured in figure 12(*a*) where contours of $\partial v'/\partial x$ coincide with c'_{xy}. The resulting perturbation in the polymer stress is τ'_{xy}, and the associated polymer work $\mathscr{W}_{yy(x)}$ is negative as demonstrated by the negative correlation between v' and $\partial\tau'_{xy}/\partial x$ in figure 12(*b*). This polymer work term therefore extracts energy from $\overline{v'v'}$. The impact is important because a weaker $\overline{v'v'}$ leads to a decrease in the production of

https://doi.org/10.1017/jfm.2014.586 Published online by Cambridge University Press

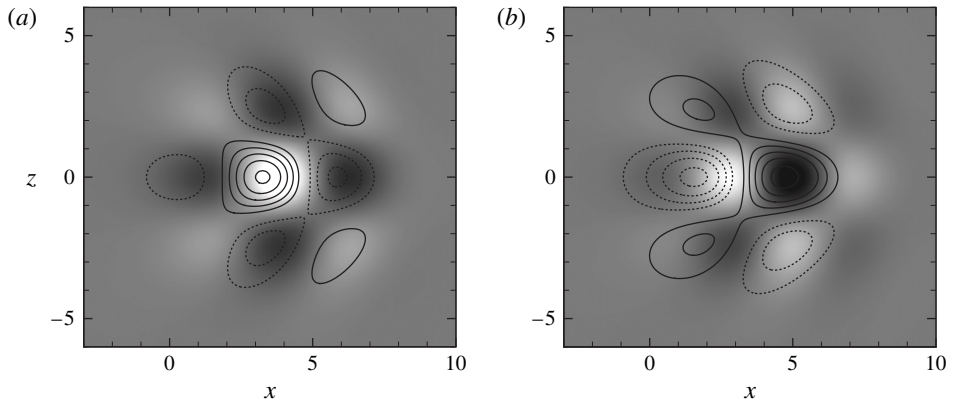


FIGURE 12. Snapshots at $t = 4$, $y = -0.56$ during the evolution of the small-amplitude vortex pair in non-Newtonian flow at $We = 40$, $L_{max} = 300$ and $\beta = 0.9$. (*a*) Contour lines, $\partial v'/\partial x$ (contour spacing 5×10^{-6}); flood, c'_{xy} (contour range $[-0.6, 0.6]$). (*b*) Contour lines, v' (contour spacing 5×10^{-6}); flood, $\partial \tau'_{xy}/\partial x$ (contour range $[-2 \times 10^{-2}, 2 \times 10^{-2}]$).

the Reynolds shear stress $\overline{u'v'}$ and, in turn, in the production of $\overline{u'u'}$ which is the principal contributor to energy amplification.

The two terms $\mathscr{W}_{zz(x)}$ and $\mathscr{W}_{yy(x)}$ are dominant because they are associated with perturbations to the mean streamwise polymer stress. In the limit of streamwise-independent disturbances, however, both terms vanish and, as a result, they were not part of the energy analysis by Hoda *et al.* (2009). In that work, the streamwise polymer-work term makes the leading contribution, and acts to increase the energy amplification which is consistent with the sign of W_{xx} in the current simulations (see figure 8).

In summary, the polymer work plays a dual role in reducing the disturbance energy in the current flow configuration, with both effects acting on the streamwise vortex: first, a direct effect is due to the negative spanwise polymer work $\widehat{\mathscr{W}_{zz}}$ on $\overline{w'w'}$. Second, an indirect effect is via the wall-normal $\widehat{\mathscr{W}_{yy}}$ term which suppresses $\overline{v'v'}$ and, as a result, the production of $\overline{u'v'}$ and ultimately of the disturbance kinetic energy.

3.2. *Influence of elasticity beyond* $We/L_{max} \sim 0.5$

The stabilizing influence of the polymer in terms of suppressing energy amplification was discussed above. Figure 6, however, also shows that this effect is reduced for $We/L_{max} > 0.5$. This is a result of the nonlinear dependence of the polymer stress on the polymer conformation for the FENE-P model and is illustrated below.

In the previous section, energy suppression was explained in terms of the perturbations to the conformation tensor, c'_{xz} and c'_{xy}, which arise due to the vorticity perturbation acting on the mean conformation. The elastic effect of the polymer is fed back to the velocity field through the polymer stress. Using the simplification (3.6) for the polymeric stress perturbation, the evolution of τ'_{xz} is governed by,

$$\left(\frac{\partial}{\partial t} + U\frac{\partial}{\partial x}\right)\tau'_{xz} \approx \frac{\partial w'}{\partial x}\frac{C_{xx}}{We}\left(1 + \frac{C_{kk}}{L^2_{max}}\right) \approx \frac{\partial w'}{\partial x}\overline{\tau}_{xx}. \tag{3.15}$$

https://doi.org/10.1017/jfm.2014.586 Published online by Cambridge University Press

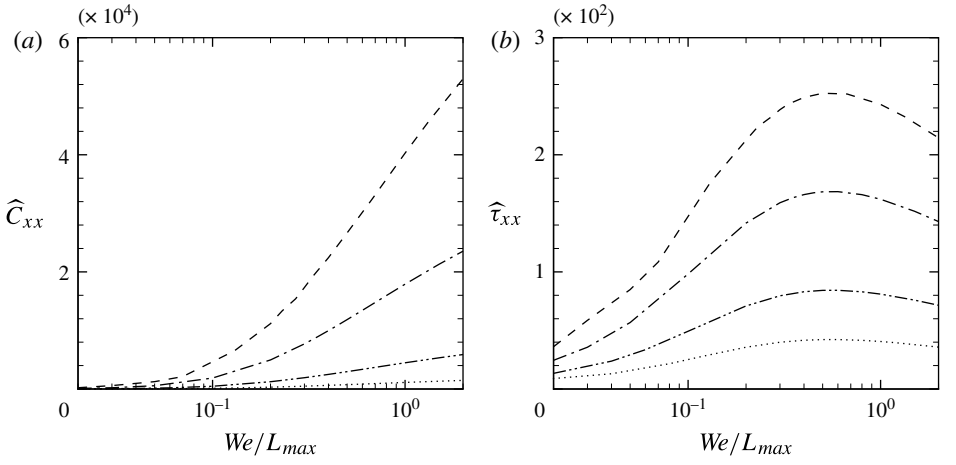


FIGURE 13. Variation of 'xx' component of the mean conformation tensor and polymeric stress tensor: ····, $L_{max}=50$; — · · —, $L_{max}=100$; — · —, $L_{max}=200$; - - - -, $L_{max}=300$.

A similar expression governs the early time behaviour of τ'_{xy},

$$\left(\frac{\partial}{\partial t}+U\frac{\partial}{\partial x}\right)\tau'_{xy}\approx\frac{\partial v'}{\partial x}\overline{\tau}_{xx}. \tag{3.16}$$

The perturbation stress therefore arises due to the action of the vorticity disturbance onto the mean stress, in analogy to the conformation. Figure 13 shows the dependence of $\widehat{C}_{xx}$ and $\widehat{\tau}_{xx}$ on We/L_{max}. While the mean conformation tensor increases monotonically with increasing We/L_{max}, the mean stress tensor reaches a maxima at $We/L_{max}\sim 0.5$. In a sense, the reservoir of mean stress from which the perturbation stress, and consequently polymer work, are extracted diminishes (similar behaviour was observed in mixing layers by Ray & Zaki 2014). Beyond the maxima, $\widehat{\tau}_{xx}$ decreases and as a result the perturbations τ'_{xz} and τ'_{xy} also decrease, which weakens the polymer work, or the influence of elasticity.

3.3. *Effect of increasing polymer concentration*

For all of the results reported so far, a solution with low polymer concentration has been considered, $\beta=0.9$. In a solution with higher polymer concentration, or a lower β, the effects of the polymer are expected to be enhanced, and the results indicate that this is indeed the case as shown in figure 14.

The energy analysis reveals that the mechanism for energy suppression remains unchanged, and that the enhanced effect of the polymer is primarily due to the corresponding increase in the magnitude of the polymer work, which was previously identified as the cause of the reduced energy amplification. This is illustrated in figure 15 where the magnitude of polymer work is shown to increase with polymer concentration.

4. Nonlinear evolution

A high-amplitude initial disturbance leads to a regime of nonlinear development beyond a short-lived initial linear phase. Results from the evolution of disturbances

https://doi.org/10.1017/jfm.2014.586 Published online by Cambridge University Press

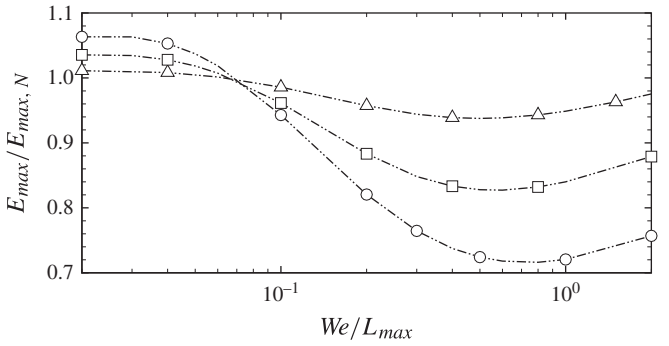


FIGURE 14. The effect of polymer concentration, represented by β, on the maximum perturbation energy in non-Newtonian flow: △, $\beta = 0.9$; □, $\beta = 0.7$; ○, $\beta = 0.5$.

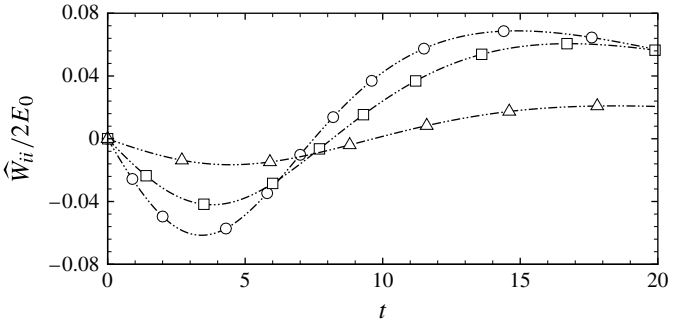


FIGURE 15. The effect of β on polymer work during the evolution of the small amplitude vortex pair at $We = 30$ and $L_{max} = 100$: △, $\beta = 0.9$; □, $\beta = 0.7$; ○, $\beta = 0.5$.

with amplitudes sufficiently large to cause nonlinear growth are presented by Henningson *et al.* (1993) for the Newtonian flow ($\epsilon = 0.10485$ for the moderate-amplitude disturbance and $\epsilon = 0.2097$ for the large-amplitude disturbance). The authors state that the nonlinear regime is characterized by pronounced streaky structures in the streamwise direction. Streak amplification can be understood in the linear growth limit by the lift-up mechanism (Landahl 1975). In the current flow configuration, the moderate- and large-amplitude localized disturbances generate, by nonlinear interactions, low-frequency components that lead to the emergence of more pronounced streaky structures via the lift-up mechanism (see figure 16). While the streaks decay in the case of the moderate amplitude disturbance, breakdown to turbulence is initiated in the case of the large-amplitude disturbance via a roll-up mechanism. As a result, a turbulent spot is formed (figure 17) and spreads thus leading to fully turbulent flow.

4.1. *Evolution of the moderate amplitude vortex pair in non-Newtonian flow*

The normalized energy amplification, $E(t)/E_0$, in the case of a moderate-amplitude vortex pair is shown in figure 18. The three curves correspond to the linear and nonlinear evolutions of the Newtonian case, and the nonlinear energy growth of the polymeric flow. The parameters $We = 15$ and $L_{max} = 100$ were selected for the viscoelastic fluid since they are comparable to those used in previous studies of fully

https://doi.org/10.1017/jfm.2014.586 Published online by Cambridge University Press

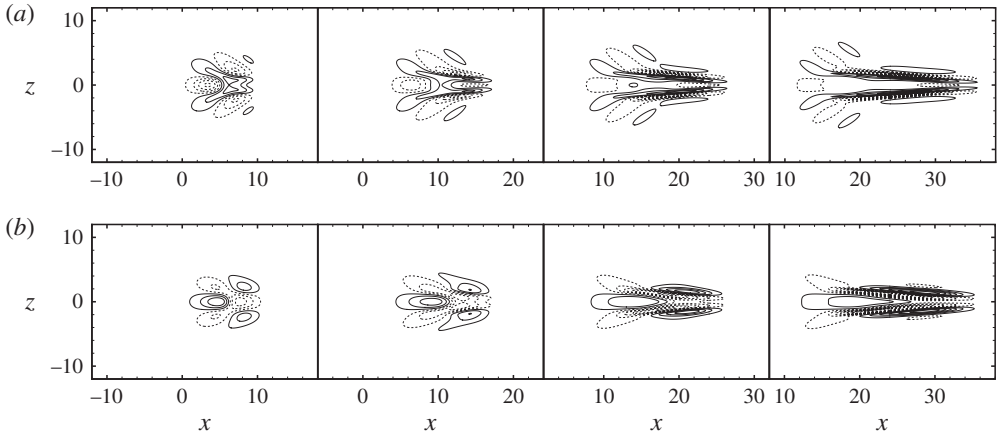


FIGURE 16. Evolution of the disturbance ($\epsilon = 0.10485$) in Newtonian flow at $y = -0.56$ and $t = \{7, 13, 20, 27\}$; (a) wall-normal v' and (b) streamwise u' velocity perturbations.

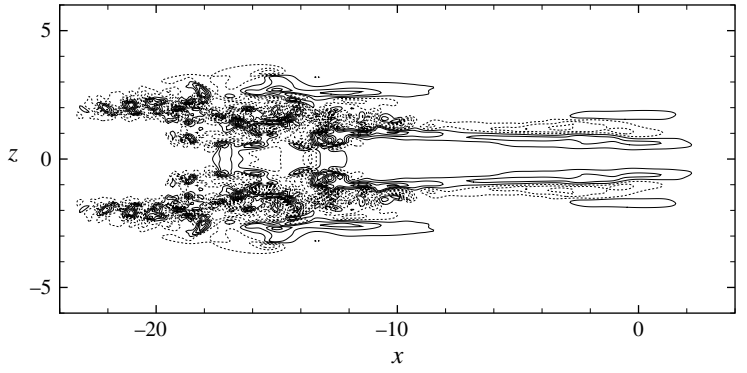


FIGURE 17. Turbulent spot in contours of v' at $t = 40$ and $y = -0.56$ during the evolution of a large vortex pair ($\epsilon = 0.2097$) in Newtonian flow. Contour spacing 3.75×10^{-2}.

turbulent non-Newtonian channel flow (Dimitropoulos *et al.* 1998; Dubief *et al.* 2004; Dallas *et al.* 2010).

At early times, $t \lesssim 10$, the linear and nonlinear simulations are in agreement. Beyond $t = 10$, the nonlinear energy growth departs from the curve for the linear evolution. For the non-Newtonian flow, there is a substantial reduction in the nonlinear growth phase. This phase is characterized by streaky structures with high streamwise perturbation velocity. The energy suppression suggests that these structures are weakened in the non-Newtonian case. The three components of polymer work are evaluated in figure 19. During the initial linear growth, the mechanism discussed for the evolution of the small amplitude vortex pair is applicable: namely the influence of negative spanwise and wall-normal polymer work.

Beyond $t = 30$, a negative streamwise component of polymer work dominates and acts to oppose the growth of streaks (figure 19). A snapshot of the instantaneous negative polymer work and its correlation with the streaky structures in the flow at $t = 40$ is shown in figure 20. In the figure, I and II are isosurfaces of the positive and negative streaks respectively, staggered in the spanwise direction such that II is closer

https://doi.org/10.1017/jfm.2014.586 Published online by Cambridge University Press

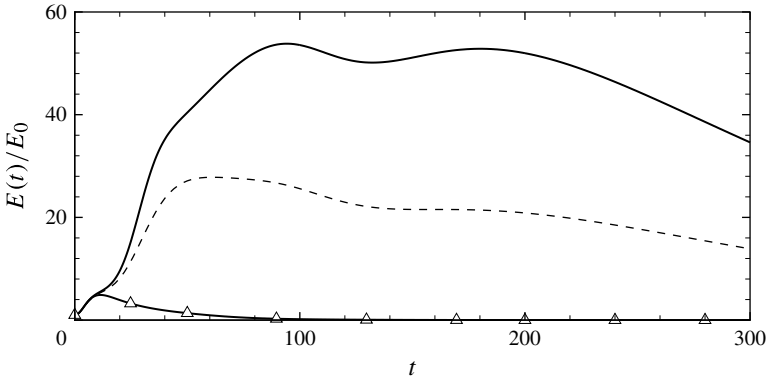


FIGURE 18. Evolution of energy amplification for $\epsilon = 0.10485$: ——, Newtonian flow; - - - -, non-Newtonian flow at $L_{max} = 100$, $\beta = 0.9$ and $We = 15$; △, $\epsilon = 0.00015$.

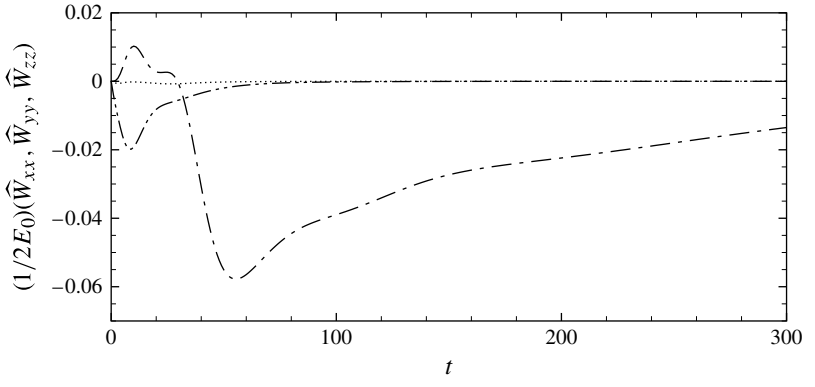


FIGURE 19. Evolution of the components of polymer work for $\epsilon = 0.10485$, $We = 15$, $L_{max} = 100$ and $\beta = 0.9$: — · —, $\widehat{\mathscr{W}_{xx}}$; · · · ·, $\widehat{\mathscr{W}_{yy}}$; — · · —, $\widehat{\mathscr{W}_{zz}}$.

to the central x–y plane of the channel. The isosurfaces are coloured with the negative streamwise polymer work that dominates during this nonlinear growth phase. There is a region of strong negative streamwise polymer work aligned along each streaky structure in the flow, illustrating a strong correlation between the streaky structures and $\mathscr{W}_{xx} < 0$. This correlation supports the hypothesis that the streamwise polymer work suppresses streaks during this early phase of nonlinear growth, consistent with the suppression in the perturbation energy. The weakening of streaks due to viscoelasticity has also been observed in the fully turbulent regime in previous studies (Dallas *et al.* 2010), especially at Weissenberg numbers which match those examined in the current simulations. With weaker streamwise streaks, transition to turbulence is expected to be prolonged in viscoelastic flow: a phenomenon which we examine next.

4.2. *Breakdown to turbulence in non-Newtonian flow*

For the moderate-amplitude vortex pair case, the formation of streaks is followed by disturbance decay and the flow returns to a laminar state. A higher-amplitude initial

https://doi.org/10.1017/jfm.2014.586 Published online by Cambridge University Press

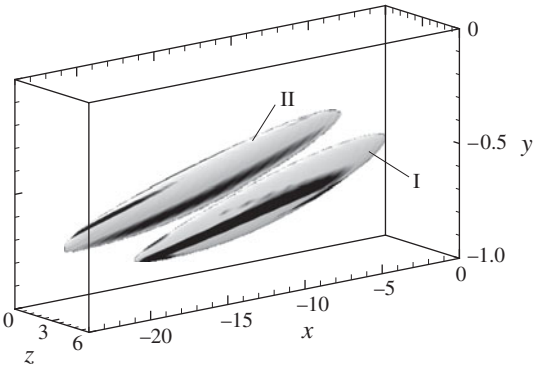


FIGURE 20. Isosurfaces of the streamwise perturbation velocity (I, $u' = 0.2$; and II, $u' = -0.2$), coloured by the streamwise polymer work at $t = 40$. Contour levels range from $\mathscr{W}_{xx}/2E_0 = -3.3$ (black) to $\mathscr{W}_{xx}/2E_0 = -1.1$ (white).

disturbance ($\epsilon = 0.2097$) is required to cause breakdown to turbulence as reported by Henningson *et al.* (1993) for Newtonian flow. In response, the disturbance evolution follows the same stages of growth described for the two lower-amplitude disturbances, but continues to amplify beyond the formation of streaks, and supports the formation of a turbulent spot.

Snapshots of u' and v' at $t = 50$ during the evolution of a large-amplitude vortex pair in Newtonian flow capture the shape of the spot (figure 21*a*,*b*). At this time instance, the spot has returned to the centre of the domain due to the periodic boundary conditions. The spot can be divided into two parts: upstream of $x = 0$, the spot is composed primarily of small-scale structures; downstream of $x = 0$, the spot consists of large-scale structures oriented in the streamwise direction. The upstream region is more appreciably altered by the presence of the polymer in the non-Newtonian flow (figure 21*c*,*d*), and the small-scale structures are visibly suppressed. The large-scale structures downstream of $x = 0$ are still present, although at a lower magnitude. In Newtonian flow, the turbulent spot represents a region in which a statistically stationary turbulent state is approached (Henningson & Kim 1991). Adopting an analogous view in the non-Newtonian flow, and based on the observed changes to the turbulent spots, it is expected that the velocity perturbations in the eventual turbulent state will be significantly weaker. This prediction is in agreement with existing literature on fully turbulent non-Newtonian flow (e.g. Dubief *et al.* 2004; Dallas *et al.* 2010).

In Newtonian flow, the high-frequency region of the turbulent spot upstream of $x = 0$ in figure 21 spreads and leads to fully turbulent flow in the entire channel. In the case of non-Newtonian flow, the perturbation velocity in that region is suppressed, and the late stages of the transition process whereby the turbulence spreads, fills the channel and becomes statistically stationary is substantially delayed. This delay is demonstrated in figures 22 and 23. In the former, the friction Reynolds number, $Re_\tau \equiv u_\tau h/\nu$ where u_τ is the friction velocity, is plotted as a function of time. The Newtonian curve rises from the initial laminar level to the turbulent state in a relatively short period of time. Beyond $t \sim 250$, a fully turbulent state is maintained throughout the computational domain. The prolonged transition to turbulence in the non-Newtonian case is reflected in the longer time for Re_τ to level off, $t > 800$, even though its final level indicates a reduced-drag state. Snapshots of the polymeric flow during the

https://doi.org/10.1017/jfm.2014.586 Published online by Cambridge University Press

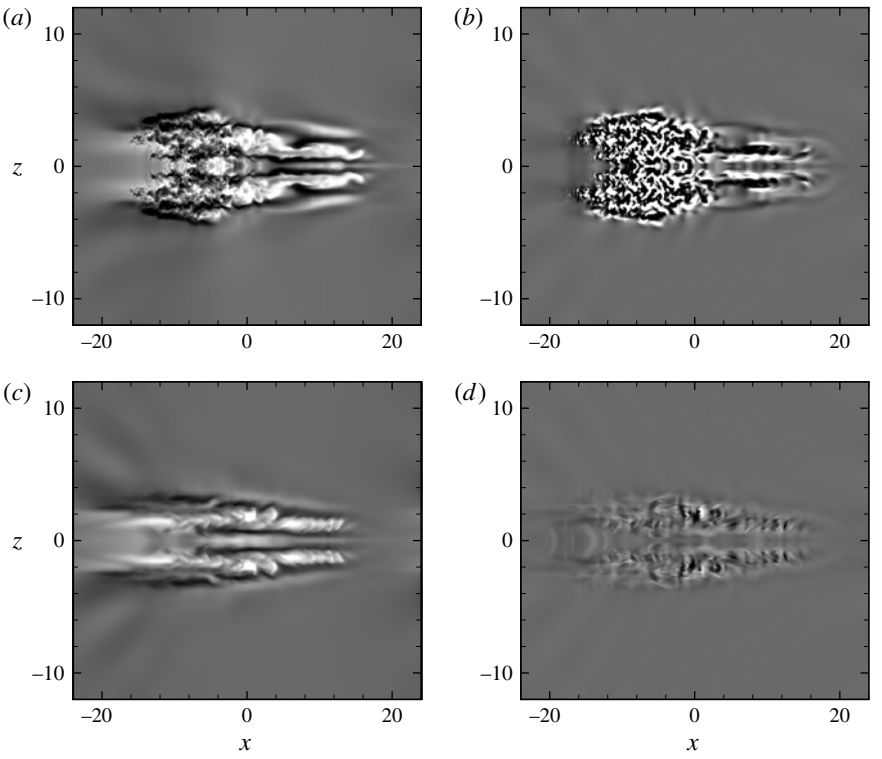


FIGURE 21. Snapshots of perturbation velocity at $t = 50$ and $y = -0.56$ during the evolution of the large-amplitude vortex pair. Newtonian flow: (*a*) $u' = [-0.3, 0.3]$; (*b*) $v' = [-0.05, 0.05]$. Non-Newtonian flow at $We = 15$, $L_{max} = 100$ and $\beta = 0.9$: (*c*) u'; (*d*) v' with the same contour limits.

transition process in figure 23 demonstrate the slow spreading of velocity perturbations across the channel. When a fully turbulent state is achieved, it differs significantly from that in Newtonian flow, as seen in figure 23(*d*,*e*), respectively.

Ultimately the non-Newtonian flow reaches a drag-reduced turbulent state, close to the maximum drag reduction (MDR) state described by the Virk asymptote (Virk & Mickley 1970). Statistics from the turbulent regime, $t > 800$, are plotted in figure 24. The mean velocity profile for the non-Newtonian flow (figure 24*a*) matches that of the Newtonian flow in the viscous sublayer. However, in the log layer, its slope is significantly increased. A drag reduction of 40 % is achieved in the current simulations. The r.m.s. velocity perturbations are compared to the Newtonian curves in figure 24(*b*). All three components of velocity have a weaker disturbance field in the polymeric flow. The recorded reduction in the r.m.s. is consistent with earlier work on drag-reduced flows (e.g. White & Mungal 2008). The statistics in figure 24 are also consistent with those in the elasto-inertial turbulence regime (Dubief, Terrapon & Soria 2013; Samanta *et al.* 2013) where the authors report the formation of sheet-like structures of polymer extension which are large in the streamwise and spanwise dimensions. Structures with similar physical size are also established in the fully turbulent state of the current study. Since our computational domain is approximately five times larger in each of the horizontal directions, the structures are observed to occupy only a fraction of the channel width.

https://doi.org/10.1017/jfm.2014.586 Published online by Cambridge University Press

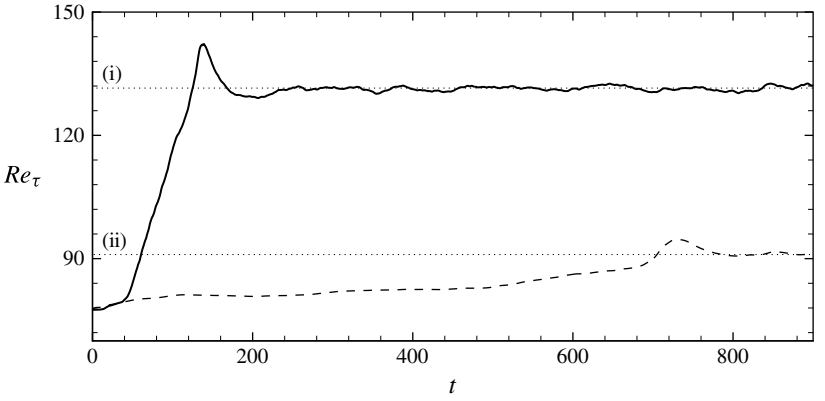


FIGURE 22. Effect of the addition of polymers to the process of transition: ——, Newtonian; - - - -, non-Newtonian at $We = 15$, $L_{max} = 100$ and $\beta = 0.9$. The dotted lines mark Re_τ in fully turbulent flow for the Newtonian (i) and non-Newtonian (ii) cases.

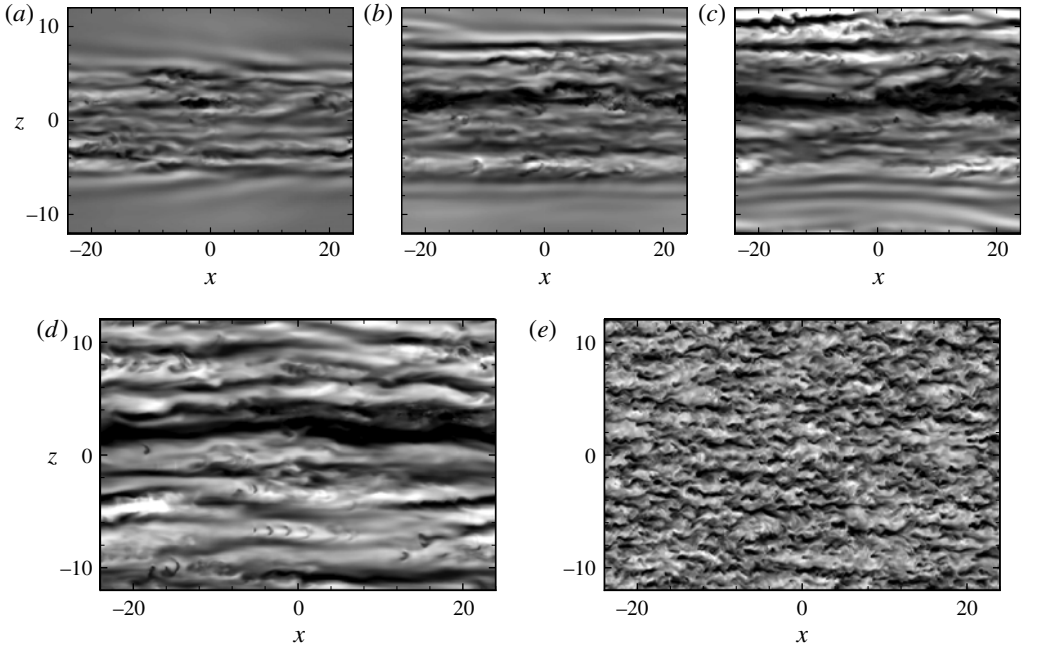


FIGURE 23. Snapshots of u' at $y = -0.56$ during the evolution of the large-amplitude vortex pair: (*a–c*) non-Newtonian flow during transition at $We = 15$, $L_{max} = 100$, $\beta = 0.9$ and $t = \{200, 400, 600\}$; (*d*) and (*e*) are a comparison of non-Newtonian and Newtonian flows, respectively, at $t = 900$. Contour limits: $[-0.2, 0.2]$.

The current simulations are performed at $Re = 2000$. Breakdown to turbulence in viscoelastic channel flow in the low-Reynolds-number regime where elastic forces are strong (Shaqfeh 1996) is largely unexplored. Recent linear theory (Jovanovic & Kumar 2011) and experiments (Pan *et al.* 2013) demonstrate the potential for significant energy amplification and nonlinear subcritical instabilities in channel flow

https://doi.org/10.1017/jfm.2014.586 Published online by Cambridge University Press

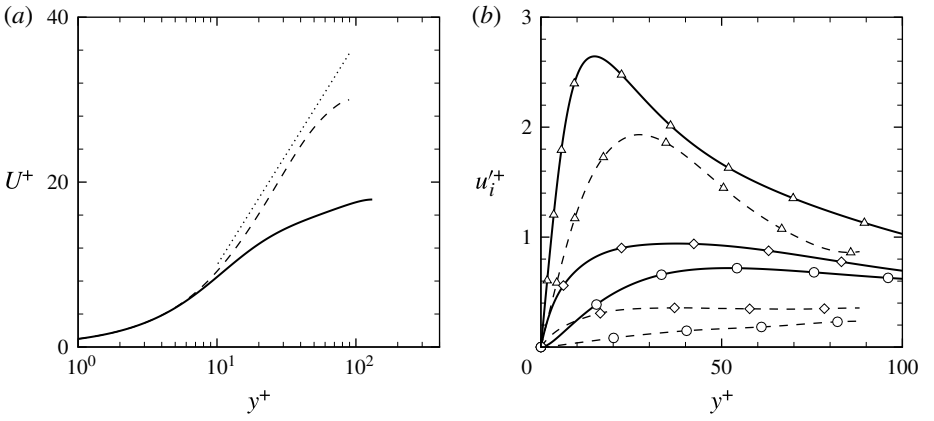


FIGURE 24. Statistics from fully turbulent flow: ——, Newtonian; - - - -, non-Newtonian at $We = 15$, $L_{max} = 100$ and $\beta = 0.9$; (*a*) mean velocity profiles; ····, Virk asymptote for MDR; (*b*) root-mean-squared velocity fluctuations; △, streamwise; ◇, spanwise; ○, wall-normal.

at $Re \ll 1$. Future DNS of transition at low Reynolds number would complement these efforts.

5. Conclusion

This study is the first to detail the laminar-to-turbulence transition process in polymeric channel flow starting from a mathematically well-defined and reproducible disturbance. The numerical simulations capture the complete evolution of the disturbance until breakdown to turbulence. An energy analysis provides an explanation of the influence of polymer additives on the transition process which can be broadly divided into three phases. During the first linear phase, energy growth takes place via the lift-up mechanism. The wall-normal and spanwise vorticity perturbations tilt the mean conformation C_{xx} and generate c'_{xz} and c'_{xy} components. This results in negative polymer work which acts to suppress the spanwise and wall-normal components of perturbation velocity. Both effects lower the rate of energy growth in the linear stage, the former directly and the later indirectly by reducing the production of $\overline{u'v'}$ and in turn of $\overline{u'u'}$. This is in agreement with the results for non-modal behaviour reported by Hoda *et al.* (2008) and Zhang *et al.* (2013). The lift-up mechanism results in the formation of streaky structures with high streamwise velocity perturbation, which are weakened by elasticity.

During the second phase, there is a significant growth of the streamwise streaks which reach high amplitude and nonlinear effects become important. During this stage, a negative streamwise polymer work weakens the streaky structures, causing a significant reduction in energy growth. The final step of transition is the formation of a turbulent spot, or breakdown to turbulence. The spot consists of a spectrum of flow structures: the streamwise-oriented structures from the preceding phase persist while small-scale structures are suppressed in the non-Newtonian flow. This leads to further suppression in the rate of energy growth and the transition process is prolonged. This delay in establishing turbulence motivates future studies of the influence of polymers on the secondary instability of the flow. The turbulent state which is established at long time is a drag-reduced state, close to the MDR asymptote.

https://doi.org/10.1017/jfm.2014.586 Published online by Cambridge University Press

The analysis of transition in the non-Newtonian flow has shed light on the effect of viscoelasticity on the linear and nonlinear stages. By focusing on an isolated initial disturbance, an uncluttered view of the transition process is possible and the disturbance evolution is examined in detail. The results from the late stages, or the nonlinear regime, naturally complement existing studies of viscoelastic turbulent channel flow.

REFERENCES

BAYLY, B. J., ORSZAG, S. A. & HERBERT, T. 1988 Instability mechanisms in shear-flow transition. *Annu. Rev. Fluid Mech.* **20**, 359–391.

BREUER, K. S. & LANDAHL, M. T. 1990 The evolution of a localized disturbance in a laminar boundary layer. Part 2. Strong disturbances. *J. Fluid Mech.* **220**, 595–621.

DALLAS, V., VASSILICOS, J. C. & HEWITT, G. F. 2010 Strong polymer–turbulence interactions in viscoelastic turbulent channel flow. *Phys. Rev.* E **82**, 066303.

DE ANGELIS, E., CASCIOLA, C. M. & PIVA, R. 2002 DNS of wall turbulence: dilute polymers and self-sustaining mechanisms. *Comput. Fluids* **31** (4–7), 495–507.

DIMITROPOULOS, C. D., SURESHKUMAR, R. & BERIS, A. N. 1998 Direct numerical simulation of viscoelastic turbulent channel flow exhibiting drag reduction: effect of the variation of rheological parameters. *J. Non-Newtonian Fluid Mech.* **79**, 433–468.

DUBIEF, Y., TERRAPON, V. E. & SORIA, J. 2013 On the mechanism of elasto-inertial turbulence. *Phys. Fluids* **25**, 110817.

DUBIEF, Y., TERRAPON, V. E., WHITE, C. M., SHAQFEH, E. S. G., MOIN, P. & LELE, S. K. 2005 New answers on the interaction between polymers and vortices in turbulent flows. *Flow Turbul. Combust.* **74**, 311–329.

DUBIEF, Y., WHITE, C. M., TERRAPON, V. E., SHAQFEH, E. S. G., MOIN, P. & LELE, S. K. 2004 On the coherent drag-reducing and turbulence-enhancing behaviour of polymers in wall flows. *J. Fluid Mech.* **514**, 271–280.

EL-KAREH, A. W. & LEAL, L. G. 1989 Existance of solutions for all Deborah numbers for a non-Newtonian model modified to include diffusion. *J. Non-Newtonian Fluid Mech.* **33**, 257–287.

HENNINGSON, D. S. & ANDERSSON, P. H. 1987 The wave structure of turbulent spots in plane Poiseuille flow. *J. Fluid Mech.* **178**, 405–421.

HENNINGSON, D. S. & KIM, J. 1991 On turbulent spots in plane Poiseuille flow. *J. Fluid Mech.* **228**, 183–205.

HENNINGSON, D. S., LUNDBLADH, A. & JOHANSSON, A. V. 1993 A mechanism for bypass transition from localized disturbances in wall-bounded shear flows. *J. Fluid Mech.* **250**, 169–207.

HODA, N., JOVANOVIC, M. R. & KUMAR, S. 2008 Energy amplification in channel flows of viscoelastic fluids. *J. Fluid Mech.* **601**, 407–424.

HODA, N., JOVANOVIC, M. R. & KUMAR, S. 2009 Frequency responses of streamwise-constant perturbations in channel flows of Oldroyd-B fluids. *J. Fluid Mech.* **625**, 411–434.

JOVANOVIC, M. R. & KUMAR, S. 2011 Nonmodal amplification of stochastic disturbances in strongly elastic channel flows. *J. Non-Newtonian Fluid Mech.* **166**, 755–778.

LANDAHL, M. T. 1975 Wave breakdown and turbulence. *SIAM J. Appl. Maths* **28**, 735–756.

LI, C.-F., SURESHKUMAR, R. & KHOMAMI, B. 2006 Influence of rheological parameters on polymer induced turbulent drag reduction. *J. Non-Newtonian Fluid Mech.* **140**, 23–40.

MIN, T., YOO, J. Y. & CHOI, H. 2001 Effect of spatial discretization schemes on numerical solutions of viscoelastic fluid flows. *J. Non-Newtonian Fluid Mech.* **100**, 27–47.

MIN, T., YOO, J. Y. & CHOI, H. 2003*a* Maximum drag reduction in a turbulent channel flow by polymer additives. *J. Fluid Mech.* **492**, 91–100.

MIN, T., YOO, J. Y., CHOI, H. & JOSEPH, D. D. 2003*b* Drag reduction by polymer additives in a turbulent channel flow. *J. Fluid Mech.* **486**, 213–238.

https://doi.org/10.1017/jfm.2014.586 Published online by Cambridge University Press

ORSZAG, S. A. 1971 Accurate solution of the Orr–Sommerfeld stability equation. *J. Fluid Mech.* **50**, 689–703.

ORSZAG, S. A. & KELLS, L. C. 1980 Transition to turbulence in plane Poiseuille and plane Couette flow. *J. Fluid Mech.* **96**, 159–205.

PAGE, J. & ZAKI, T. A. 2014 Streak evolution in viscoelastic Couette flow. *J. Fluid Mech.* **742**, 520–551.

PAN, L., MOROZOV, A., WAGNER, C. & ARRATIA, P. E. 2013 Nonlinear elastic instability in channel flows at low Reynolds numbers. *Phys. Rev. Lett.* **110**, 174502.

RAY, P. K. & ZAKI, T. A. 2014 Absolute instability in viscoelastic mixing layers. *Phys. Fluids* **26**, 014103.

RICHTER, D., IACCARINO, G. & SHAQFEH, E. S. G. 2010 Simulations of three-dimensional viscoelastic flows past a circular cylinder at moderate Reynolds numbers. *J. Fluid Mech.* **651**, 415–442.

SAMANTA, D., DUBIEF, Y., HOLZNER, M., SCHAFER, C. & MOROZOV, A. N. 2013 Elasto-inertial turbulence. *Proc. Natl Acad. Sci. USA* **110**, 10557–10562.

SHAQFEH, E. S. G. 1996 Purely elastic instabilities in viscometric flows. *Annu. Rev. Fluid Mech.* **28**, 129–185.

STONE, P. A., WALEFFE, W. & GRAHAM, M. D. 2002 Toward a structural understanding of turbulent drag reduction: nonlinear coherent states in viscoelastic shear flows. *Phys. Rev. Lett.* **89**, 208301.

SURESHKUMAR, R. & BERIS, A. N. 1995 Effect of artificial stress diffusivity on the stability of numerical calculations and the flow dynamics of time-dependent viscoelastic flows. *J. Non-Newtonian Fluid Mech.* **60**, 53–80.

SURESHKUMAR, R., BERIS, A. N. & HANDLER, R. A. 1997 Direct numerical simulation of the turbulent channel flow of a polymer solution. *Phys. Fluids* **9**, 743–755.

TOMS, B. 1948 Observation on the flow of linear polymer solutions through straight tubes at large Reynolds numbers. In *Proceedings of the International Rheological Congress*, vol. 2 pp. 135–141.

TSUKAHARA, T., ISHIGAMI, T., YU, B. & KAWAGUCHI, Y. 2011 DNS study on viscoelastic effect in drag-reduced turbulent channel flow. *J. Turbul.* **12**, 1–25.

VAITHIANATHAN, T. & COLLINS, L. R. 2003 Numerical approach to simulating turbulent flow of a viscoelastic polymer solution. *J. Comput. Phys.* **187**, 1–21.

VIRK, P. S. & MICKLEY, H. S. 1970 The ultimate asymptote and mean flow structures in Tom's phenomenon. *Trans. ASME E: J. Appl. Mech.* **37**, 488–493.

WHITE, C. M. & MUNGAL, M. G. 2008 Mechanics and prediction of turbulent drag reduction with polymer additives. *Annu. Rev. Fluid Mech.* **40**, 235–256.

XI, L. & GRAHAM, M. D. 2010 Turbulent drag reduction and multistage transitions in viscoelastic minimal flow units. *J. Fluid Mech.* **647**, 421–452.

XI, L. & GRAHAM, M. D. 2012 Intermittent dynamics of turbulence hibernation in Newtonian and viscoelastic minimal channel flows. *J. Fluid Mech.* **693**, 433–472.

YU, B., LI, F. & KAWAGUCHI, Y. 2004 Numerical and experimental investigation of turbulent characteristics in a drag-reducing flow with surfactant additives. *Intl J. Heat Fluid Flow* **25**, 961–974.

ZHANG, M., LASHGARI, I., ZAKI, T. A. & BRANDT, L. 2013 Linear stablity analysis of channel flow of viscoelastic Oldroyd-B and FENE-P fluids. *J. Fluid Mech.* **737**, 249–279.

ZHOU, Q. & AKHAVAN, R. 2003 A comparison of FENE and FENE-P dumbbell and chain models in turbulent flow. *J. Non-Newtonian Fluid Mech.* **109**, 115–155.

https://doi.org/10.1017/jfm.2014.586 Published online by Cambridge University Press